Modulation of Wind Work by Oceanic Current Interaction with the Atmosphere

Lionel Renault, M. Jeroen Molemaker, James C. McWilliams,
and Alexander F. Shchepetkin

*Department of Atmospheric and Oceanic Sciences, University of California, Los Angeles,
Los Angeles, California*

Florian Lemarié

INRIA, Université Grenoble-Alpes, CNRS, LJK, Grenoble, France

Dudley Chelton

*College of Earth, Ocean, and Atmospheric Sciences, Oregon State University,
Corvallis, Oregon*

Serena Illig

*Laboratoire d'Étude en Géophysique et Océanographie Spatiale, IRD, Toulouse, France,
and Department of Oceanography, MARE Institute, University of Cape Town,
Rondebosch, South Africa*

Alex Hall

*Department of Atmospheric and Oceanic Sciences, University of California,
Los Angeles, Los Angeles, California*

ABSTRACT

In this study, uncoupled and coupled ocean–atmosphere simulations are carried out for the California Upwelling System to assess the dynamic ocean–atmosphere interactions, namely, the ocean surface current feedback to the atmosphere. The authors show the current feedback, by modulating the energy transfer from the atmosphere to the ocean, controls the oceanic eddy kinetic energy (EKE). For the first time, it is demonstrated that the current feedback has an effect on the surface stress and a counteracting effect on the wind itself. The current feedback acts as an oceanic eddy killer, reducing by half the surface EKE, and by 27% the depth-integrated EKE. On one hand, it reduces the coastal generation of eddies by weakening the surface stress and hence the nearshore supply of positive wind work (i.e., the work done by the wind on the ocean). On the other hand, by inducing a surface stress curl opposite to the current vorticity, it deflects energy from the geostrophic current into the atmosphere and dampens eddies. The wind response counteracts the surface stress response. It partly reenergizes the ocean in the coastal region and decreases the offshore return of energy to the atmosphere. Eddy statistics confirm the current feedback dampens the eddies and reduces their lifetime, improving the realism of the simulation. Finally, the authors propose an additional energy element in the Lorenz diagram of energy conversion: namely, the current-induced transfer of energy from the ocean to the atmosphere at the eddy scale.

Corresponding author address: Lionel Renault, Department of Atmospheric and Oceanic Sciences, University of California, Los Angeles, 405 Hilgard Ave., Los Angeles, CA 90095-1565.
E-mail: lrenault@atmos.ucla.edu

1. Introduction

Eastern boundary upwelling systems (EBUS), such as the California Current System (CCS), belong to the most productive coastal environments (e.g., Carr and

Kearns 2003), supporting some of the world's major fisheries (e.g., FAO 2009). The CCS upwelling and its productivity present a seasonal variability with a favorable season during spring and summer (Marchesiello et al. 2003; Renault et al. 2015), where high biological productivity is largely determined by wind-driven upwelling. As for the other EBUS (e.g., Benguela, Canary, and Humboldt), equatorward winds drive coastal upwelling, Ekman pumping, alongshore currents, and then productivity. Additionally, coastal currents and significant oceanic mesoscale variability contribute to cross-shore exchanges of heat, salt, and biogeochemical tracers between the open and coastal oceans (Marchesiello et al. 2003; Capet et al. 2008b; Gruber et al. 2011; Chaigneau et al. 2011).

Eddies generated by dynamical instabilities of the currents (Marchesiello et al. 2003) lead to lateral heat transport so that effects of coastal upwelling on sea surface temperature (SST) can be felt hundreds of kilometers away (Capet et al. 2008b). In the open ocean and, in particular, in low-nutrient environments, mesoscale processes increase the net upward flux of limiting nutrients and enhance biological production (Martin and Richards 2001; McGillicuddy et al. 2007). For the EBUS (as shown by, e.g., Carr and Kearns 2003), the net primary production (NPP) is primarily controlled by the magnitude of the upwelling favorable winds through the upwelling strength. However, Lathuilière et al. (2010), Gruber et al. (2011), and Renault et al. (2016) also show that eddies can be a limiting factor, which progressively prevent high levels of NPP as the number of eddies increase by subducting the nutrients below the euphotic layer (eddy quenching). Renault et al. (2016) show that the coastal wind shape modulates by modifying the baroclinic instabilities of the eddy kinetic energy (EKE) and therefore the eddy quenching. The eddy contribution to oceanic fluxes is substantial (Colas et al. 2013), and a realistic wind forcing is crucial to simulate the mesoscale activity realistically (Renault et al. 2016).

In the EBUS, various processes can modulate the coastal spatial pattern of the wind: for example, sharp changes of surface drag and the atmospheric boundary layer at the land–sea interface (Edwards et al. 2001; Capet et al. 2004; Renault et al. 2015); coastal orography (Edwards et al. 2001; Perlin et al. 2011; Renault et al. 2015); and SST–wind coupling (Chelton et al. 2007; Jin et al. 2009; Oerder et al. 2016; Desbiolles et al. 2016). These coastal circulation processes are essential for understanding the upwelling systems (Marchesiello et al. 2003; Capet et al. 2004; Renault et al. 2012). The ocean feedback to the atmosphere has been recently studied, mainly focusing on the thermal feedback (e.g., Chelton et al. 2004, 2007; Spall 2007; Perlin et al. 2007,

2011; Minobe et al. 2008; Jin et al. 2009; Park et al. 2006; Cornillon and Park 2001). SST gradients induce gradients in lower-atmospheric stratification; hence, gradients in vertical momentum flux in the atmospheric boundary layer and gradients in the surface wind and stress are induced beneath an otherwise more uniform midtropospheric wind. Chelton et al. (2004, 2007), using satellite observations, show approximately linear relationships between the surface stress curl (divergence) and the crosswind (downwind) components of the local SST gradient. Recent studies also highlight how a mesoscale SST front may have an impact all the way up to the troposphere (Minobe et al. 2008). The effect of oceanic currents is another aspect of interaction between atmosphere and ocean; however, its effects are not yet well known. Some work shows that the current effect on the surface stress can lead to a reduction of the EKE of the ocean via a "mechanical dampening" (Duhaut and Straub 2006; Dewar and Flierl 1987; Dawe and Thompson 2006; Hughes and Wilson 2008; Eden and Dietze 2009) and hence a reduction of the wind work. Yet, in those studies the atmospheric response to the current feedback is neglected. Recently Seo et al. (2016), using a coupled model, confirms that the current feedback induces a reduction of the work done by the wind on the ocean (wind work) that, in turn, dampens the EKE. To our knowledge, the effects of surface currents on the surface wind speed have not been yet studied. Eden and Dietze (2009) and Seo et al. (2016) can be associated with an observational analysis that shows the current-induced surface stress curl change induces Ekman pumping velocities that are of the opposite sign to the surface vorticity of the eddy, inducing its attenuation (Gaube et al. 2015).

In oceanic numerical modeling, the surface stress is usually estimated as a function of the wind speed, ignoring the fact that the ocean surface current also has a drag force on the atmosphere. Scott and Xu (2009) shows such a simplification can lead to an overestimation of the total energy input to the ocean by wind work and suggests the current should be included when estimating the surface stress. In this paper, using a set of coupled and partially coupled simulations, the focus is on this surface current feedback to the atmosphere. The objectives are to assess how the current feedback modifies the wind work and to address how it alters both the atmospheric and oceanic EKE. This raises the question of how best to force an oceanic model. Oceanic simulations forced by a prescribed wind stress inherently cannot represent the current feedback on the stress. Furthermore, although uncoupled oceanic simulations forced by an atmospheric wind product can estimate the surface

stress using the air–sea velocity difference, they cannot represent the influence of surface currents on the surface wind speed as far as we know. This point has not previously been documented.

The paper is organized as follows: Section 2 describes the model configuration and methodology. In section 3, the effect of the current feedback on the surface stress and EKE is assessed. Section 4 addresses the corresponding wind adjustment. In section 5, an eddy attenuation time scale and Ekman pumping are estimated, and a mechanistic view of the current feedback effect is presented. In section 6, an eddy statistical view allows a direct validation of our results by comparison to observations. The results are discussed in section 7, which is followed by the conclusions.

2. Model configuration and methodology

a. The Regional Oceanic Modeling System

The oceanic simulations were performed with the Regional Oceanic Modeling System (ROMS) (Shchepetkin and McWilliams 2005) in its Adapted Grid Refinement in FORTRAN (AGRIF) version (Debreu et al. 2012). ROMS is a free-surface, terrain-following coordinate model with split-explicit time stepping and with Boussinesq and hydrostatic approximations. ROMS is implemented in a configuration with two offline nested grids. The coarser grid extends from 170° to 104°W and from 18° to 62.3°N along the U.S. West Coast and is 322 × 450 points with a resolution of 12 km. Its purpose is to force the second domain. The second domain grid extends from 144.7° to 112.5°W and from 22.7° to 51.1°N (Fig. 1). The model grid is 437 × 662 points with a resolution of 4 km. The boundary condition algorithm consists of a modified Flather-type scheme for the barotropic mode (Mason et al. 2010) and Orlanski-type scheme for the baroclinic mode (including temperature and salinity; Marchesiello et al. 2001).

Bathymetry for all domains is constructed from the Shuttle Radar Topography Mission (SRTM30 plus) dataset (available at http://topex.ucsd.edu/WWW.html/srtm30.plus.html) based on the 1-min Sandwell and Smith (1997) global dataset and higher-resolution data where available. A Gaussian smoothing kernel with a width of 4 times the topographic grid spacing is used to avoid aliasing whenever the topographic data are available at higher resolution than the computational grid and to ensure the smoothness of the topography at the grid scale. Also, in order to avoid pressure gradient errors induced by terrain-following (sigma) coordinates in shallow regions with steep bathymetric slope (Beckmann and Haidvogel 1993), we apply local smoothing of the bottom topography, such as the

maximum difference between adjacent gridcell depths divided by their mean depth ($r = \Delta h/\overline{h}$). Here, local smoothing is applied where the steepness of the topography exceeds a factor $r = 0.2$.

Lateral oceanic forcing for the largest domain and surface forcing for all simulations are interannual. Temperature, salinity, surface elevation, and horizontal velocity initial and boundary information for the largest domain covering the whole North America west coast are taken from the monthly averaged Simple Ocean Data Assimilation (SODA) ocean interannual outputs (Carton and Giese 2008). Bulk formulae (Large 2006) are used to estimate the freshwater, turbulent, and momentum fluxes using the atmospheric fields derived from the uncoupled Weather Research and Forecasting (WRF) Model simulation. In the coupled simulations, the fluxes are computed by WRF and then given to ROMS using the same bulk formulae.

The 12-km domain is first spun up from the SODA initial state, 1 January 1994, for a few months, then run for an additional period until the end of 1999. Kinetic energy in the domain is statistically equilibrated within the first few months of simulation. The second grid (4-km resolution) is then nested in the parent grid from 1 June 1994. Results obtained after a 6-month spinup are then used in our analysis. All domains have 42 levels in the vertical with the same vertical grid system concentrating vertical levels near the surface (Shchepetkin and McWilliams 2009), with stretching surface and bottom parameters hcline = 250 m, $\theta b = 1.5$, and $\theta s = 6.5$. Finally, vertical mixing of tracers and momentum is done with a K-profile parameterization (KPP; Large et al. 1994). In this study, only the period 1995–99 is analyzed.

b. The Weather Research and Forecasting Model

WRF (version 3.6; Skamarock et al. 2008) is implemented in a configuration with two nested grids. The largest domain covers the North American west coast with a horizontal resolution of 18 km (not shown); the inner domain covers the U.S. West Coast, with a horizontal resolution of 6 km (see Renault et al. 2015), which is slightly larger than the ROMS 4-km grid. The coarser grid (WRF18) reproduces the large-scale synoptic features that force the local dynamics in the second grid, each using a one-way offline nesting with three-hourly updates of the boundary conditions. The coarser grid simulation (WRF18) is first run independently. It is initialized with the Climate Forecast System Reanalysis (CFSR) (≈40 km spatial resolution; Saha et al. 2010) from 1 January 1994 and integrated for 6 yr with time-dependent boundary conditions interpolated from the same three-hourly reanalysis. Forty vertical levels are used, with half of them in the lowest 1.5 km. The nested domain (WRF6) was
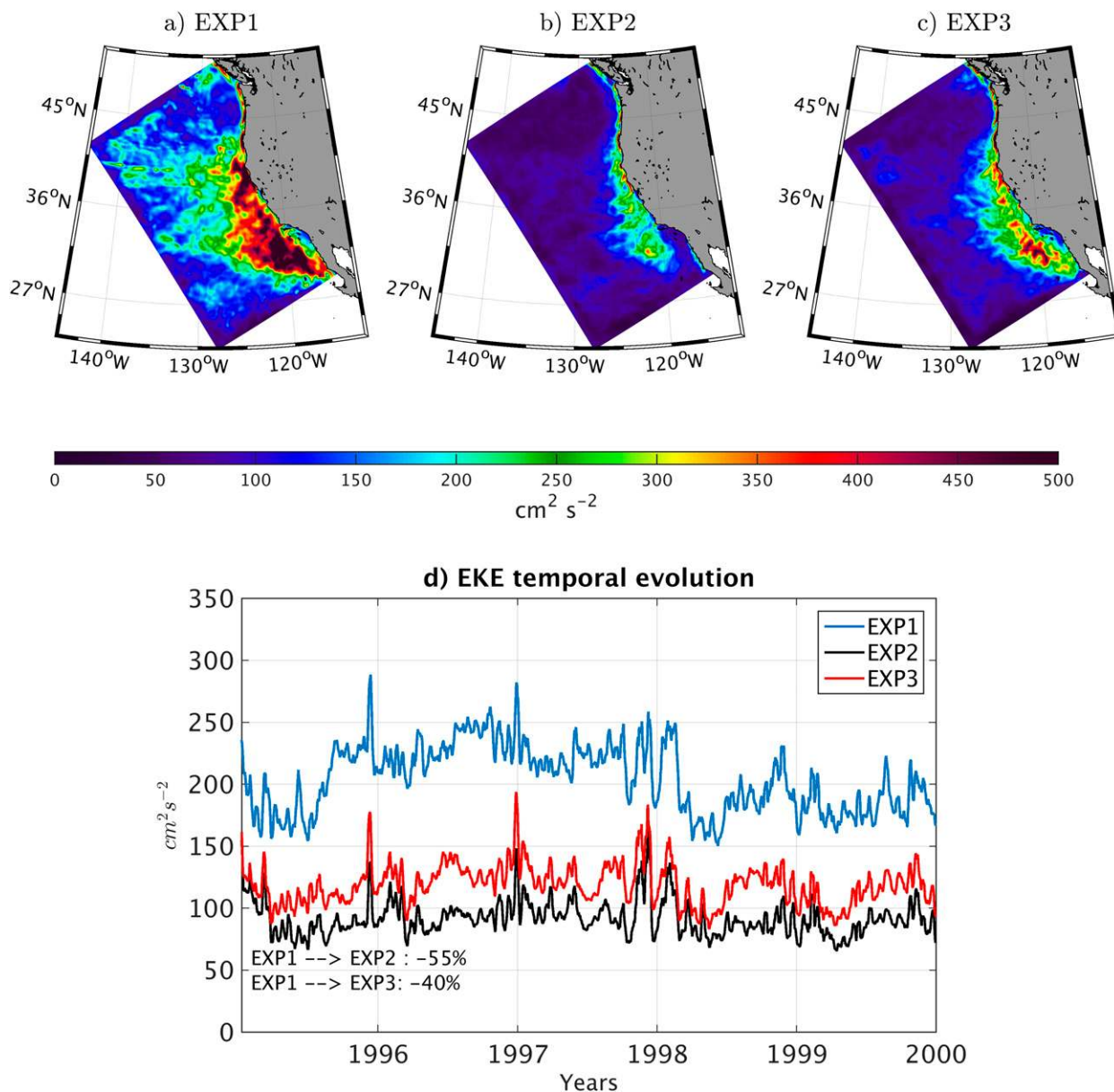
FIG. 1. (top) Mean surface EKE (cm^2 s^{-2}) from EXP1, EXP2, and EXP3. (bottom) Temporal evolution of the EKE averaged over the whole domain. The difference percentages between the uncoupled experiments and the coupled experiment are indicated. There is a reduction of the EKE when using the current to estimate the surface stress. The atmospheric response dampens the EKE reduction. From EXP1 to EXP2, the EKE is reduced by 55%, whereas from EXP1 to EXP3, the EKE is reduced by 40%.

initialized from the coarse solution WRF18 on 1 June 1994 and integrated for 5.5 yr.

A full set of parameterization schemes is included in WRF. The model configuration was set up with the following parameterizations: the WRF single-moment 6-class microphysics scheme (Hong and Lim 2006) modified to take into account the droplet concentration (Jousse et al. 2016); the Tiedtke cumulus parameterization (Zhang et al. 2011); the new Goddard scheme for shortwave and longwave radiation (Chou and Suarez 1999); the Noah land surface model (Skamarock et al. 2008); and the Mellor–Yamada–Nakanishi–Niino (MYNN2.5) planetary boundary layer (PBL) scheme (Nakanishi and Niino 2006).[1]

---

[1] Other WRF PBL schemes were tried [e.g., Yonsei University (Hong et al. 2006), University of Washington, and Park and Bretherton (2009)]. The MYNN2.5 gave, in general, more realistic features, especially in terms of cloud cover.

c. OASIS/MCT coupling procedure

The OASIS coupler (https://verc.enes.org/oasis/metrics/oasis4-dissemination) is based on the Model Coupling Toolkit (MCT; developed at Argonne National Laboratory) and supports exchanges of general two-dimensional fields between numerical codes representing different components of the climate system. All transformations, including regridding, are executed in parallel on the set of source or target component processes, and all coupling exchanges are executed in parallel directly between the components. In our configuration, every hour, WRF gives ROMS the hourly averages of freshwater, heat, and momentum fluxes; whereas, ROMS sends to WRF the hourly SST and, eventually, the surface currents.

d. Experiments

Table 1 summarizes the three experiments carried out to assess the impact of the oceanic currents on the surface stress, wind, and oceanic EKE. Experiment 1 (EXP1) is an SST coupled ROMS–WRF simulation. Experiment 2 (EXP2) is an uncoupled simulation that uses the atmosphere from EXP1 and that takes into account the oceanic surface current when estimating the surface stress. It allows us to assess the oceanic response to the current feedback. Finally, experiment 3 (EXP3) is a fully coupled simulation in the sense that it has both thermal and current feedbacks to the atmosphere. The surface stress is estimated using a bulk formula with a velocity that is the surface wind relative to the ocean surface current:

$$U = U_a - U_o, \qquad (1)$$

where U_a and U_o are the surface wind (at the first vertical level in WRF) and the surface current (at ROMS first surface level), respectively. As described by Lemarié (2015), because of the implicit treatment of the bottom boundary condition in most atmospheric models, the use of relative winds involves a modification of both the surface-layer vertical mixing parameterization (MYNN2.5 in our case) and the tridiagonal matrix for vertical turbulent diffusion.

e. EKE budget

All quantities are decomposed into the time mean estimated over the 1995–99 period and indicated with an overbar ($\overline{\cdot}$), and their deviations from this long-term mean are referred to using primes ($'$). In our analysis, the seasonal variability is not removed.

The total wind work is defined as

$$FK = \frac{1}{\rho_0}(\overline{\tau_x u_o} + \overline{\tau_y v_o}), \qquad (2)$$

TABLE 1. Sensitivity experiments.

Experiments	Current feedback
EXP1	None
EXP2	Only in surface stress, using atmosphere from EXP1
EXP3	In both surface stress and in atmosphere

where u_o and v_o are the zonal and meridional surface currents, τ_x and τ_y are the zonal and meridional surface stresses, and ρ_0 is the mean seawater density.

The geostrophic wind work is defined as

$$FK_g = \frac{1}{\rho_0}(\overline{\tau_x u_{og}} + \overline{\tau_y v_{og}}), \qquad (3)$$

where u_{og} and v_{og} are the zonal and meridional surface geostrophic currents.

As in Marchesiello et al. (2003), we focus on the following relevant energy source and eddy–mean conversion terms:

- The mean wind work,

$$F_m K_m = \frac{1}{\rho_0}(\overline{\tau_x}\,\overline{u_o} + \overline{\tau_y}\,\overline{v_o}). \qquad (4)$$

- The eddy wind work,

$$F_e K_e = \frac{1}{\rho_0}(\overline{\tau_x' u_o'} + \overline{\tau_y' v_o'}). \qquad (5)$$

- Barotropic (Reynolds stress) conversion $K_m K_e$,

$$K_m K_e = \int_z -\left(\overline{u_o' u_o'}\frac{\partial \overline{u_o}}{\partial x} + \overline{u_o' v_o'}\frac{\partial \overline{u_o}}{\partial y} + \overline{u_o' w'}\frac{\partial \overline{u_o}}{\partial z} \right. $$
$$\left. + \overline{v_o' v_o'}\frac{\partial \overline{v_o}}{\partial x} + \overline{v_o' v_o'}\frac{\partial \overline{v_o}}{\partial y} + \overline{v_o' w'}\frac{\partial \overline{v_o}}{\partial z} \right), \qquad (6)$$

where w is the vertical velocity and x, y, and z are the zonal, meridional, and vertical coordinates, respectively.

- Baroclinic conversion $P_e K_e$,

$$P_e K_e = \int_z -\frac{g}{\rho_0}\overline{\rho' w'}, \qquad (7)$$

where g is the gravitational acceleration.

The quantity $F_m K_m$ represents the transfer of energy from mean surface wind forcing to mean kinetic energy, $F_e K_e$ represents the transfer of energy from surface wind-forcing anomalies to EKE, $K_m K_e$ represents the barotropic conversion from mean kinetic energy to EKE, and $P_e K_e$ represents the baroclinic conversion from eddy available potential energy to EKE. We computed those

conversion terms at each model grid point. The wind work is estimated at the free surface, whereas the barotropic and baroclinic conversion terms are integrated over the whole water column. Cross-shore sections are evaluated using d as the cross-shore distance.

f. Eddy tracking

The eddy tracking detection method developed by Chelton et al. (2011) is used to detect and track eddies in the simulations and in the Archiving, Validation, and Interpretation of Satellite Oceanographic Data (AVISO) dataset (Ducet et al. 2000). This approach consists in detecting closed contours of sea level anomalies (SLA) that include a local extremum and several other criteria to identify and track mesoscale eddies. An eddy is viewed as a coherent isolated vortex; therefore, the corresponding SLA has the form of a bump or a depression. Before applying the eddy tracking procedure, the model outputs were first filtered by removing the seasonal cycle (annual plus semiannual components) at each grid point. In this study, we define the long-lived eddies as tracked eddies that have a continuous lifetime greater than 16 weeks. The AVISO data are only able to resolve eddies with radii longer than about 40 km (Chelton et al. 2011). Although the eddy lifetime dependence on eddy scale in the real ocean is not yet known, by focusing on eddies with long lifetimes, the resolution capability of the AVISO dataset should not be a major limitation.

3. Eddy kinetic energy and energy conversion

a. Eddy kinetic energy

The surface EKE from the different experiments is estimated using the daily surface current perturbations. The mean surface EKE and the temporal evolution of its domain average are shown in Fig. 1. In good agreement with the literature (Marchesiello et al. 2003; Renault et al. 2016), in all the experiments the EKE has larger values nearer to shore and exhibits a broad decay further offshore. EXP1 shows a relatively weak decay with high values of EKE offshore. From EXP1 to EXP2, the current feedback to the surface stress reduces the EKE by 55%, and, in particular, it strongly decreases the offshore EKE, improving the realism of the simulation [e.g., see Fig. 2 from Capet et al. (2008a)]. EXP3 also reduces the surface EKE relative to EXP1, but only by 40%, which is in good agreement with Seo et al. (2016). The atmospheric response to the reduced wind work with current feedback leads to an increase in surface wind strength (section 4b); hence, the EKE reduction observed in EXP2 is diminished. To our knowledge, this is the first time this phenomenon has been documented.

Similar conclusions can be drawn using the depth-integrated EKE: from EXP1 to EXP2, it is reduced by 35%, whereas, from EXP1 to EXP3, it is reduced by only 27%. The exclusion of an atmospheric response in EXP2 leads to an overestimation of the oceanic EKE reduction, both nearshore and offshore. The EKE reduction can be split into two processes: On one hand there is a surface stress adjustment that tends to reduce the EKE (EXP2). There is also a wind adjustment that partly counteracts the surface stress reduction, thus attenuating the EKE reduction (EXP3).

b. Energy conversion

A simplified EKE budget (section 2e) is computed to diagnose which processes lead to the EKE reduction by the current feedback. Because the time-mean quantities and then $F_m K_m$ are barely affected by the current feedback (about 1% change, not shown), Fig. 2 shows the spatial distribution of only $F_e K_e$, $P_e K_e$, and $K_m K_e$ from EXP1 (top panel) and from EXP3 (bottom panel), and Fig. 3 is the cross-shore profile for each term averaged between 30° and 45°N from EXP1, EXP2, and EXP3. As in Marchesiello et al. (2003), the baroclinic instability and the eddy wind work are the main sources of EKE, and they have higher values in the nearshore region. Note here, that $K_m K_e$ is a secondary term. The wind work is also stronger in those simulations than in Marchesiello et al. (2003), which can be attributed to the poor quality of the wind used in Marchesiello et al. (2003) [i.e., Comprehensive Ocean–Atmosphere Data Set (COADS)]: it is monthly, and in particular it does not resolve the high-frequency wind forcing (hourly here, which excites inertial currents), nor does it resolve the slackening of the winds near the coast (drop-off; e.g., Renault et al. 2016). The COADS wind stress forcing induces levels of EKE that are too low. As in Marchesiello et al. (2003), in the nearshore region, a coastal band of about 80-km width is marked by large values of $F_e K_e$. In all the experiments, the wind perturbations induce an offshore Ekman surface current and an oceanic coastal jet (e.g., Renault et al. 2009) that flows partially in the same direction as the wind, inducing a positive $F_e K_e$. Also offshore, the Ekman surface current is partly in the direction of the wind with a generally positive $F_e K_e$.

The main effect of the current feedback is a reduction of $F_e K_e$ in both the nearshore and offshore regions (Figs. 2 and 3). The oceanic surface currents can be split into their geostrophic and ageostrophic parts:

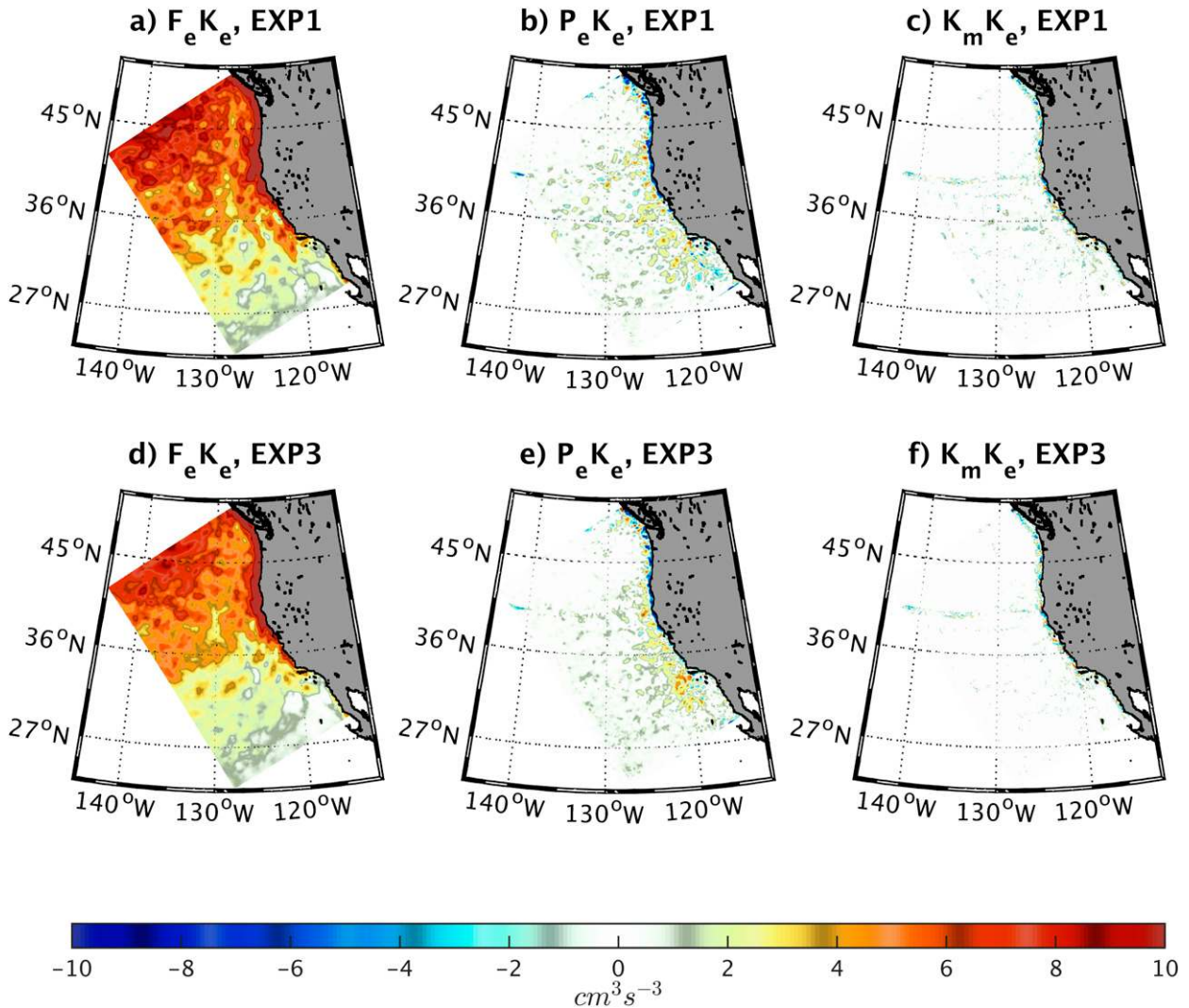$$u_o = u_{og} + u_{oa} \qquad (8)$$

and

FIG. 2. Depth-integrated EKE-budget components (cm^3 s^{-3}) from (top) EXP1 and (bottom) EXP3: (left)–(right) the eddy wind work F_eK_e, the baroclinic conversion P_eK_e, and the barotropic conversion K_mK_e. The main energy source terms are F_eK_e and P_eK_e. The reduction of the EKE in Fig. 1 is explained by the reduction of F_eK_e by the current feedback.

$$v_o = v_{og} + v_{oa}, \tag{9}$$

with u_{og}, v_{og}, u_{oa}, and v_{oa} the zonal and meridional geostrophic and ageostrophic currents, respectively. Using (8) and (9), F_eK_e can, in turn, be split into its geostrophic (F_eK_{eg}) and ageostrophic (F_eK_{ea}) parts:

$$F_eK_{eg} = \frac{1}{\rho_0}(\overline{\tau'_x u'_{og}} + \overline{\tau'_y v'_{og}}) \tag{10}$$

and

$$F_eK_{ea} = \frac{1}{\rho_0}(\overline{\tau'_x u'_{oa}} + \overline{\tau'_y v'_{oa}}). \tag{11}$$

Figure 4 shows F_eK_{eg} from EXP1 and EXP3, and Fig. 3c shows the cross-shore profile of F_eK_{eg} from EXP1,

EXP2, and EXP3. In all the experiments, the offshore positive F_eK_e is essentially due to F_eK_{ea} (more than 95%), whereas nearshore F_eK_{ea} accounts for only 37% of F_eK_e.

The induced current feedback reduction of F_eK_e mainly acts through the geostrophic currents. Offshore, the current-induced reduction of F_eK_e is due to two different mechanisms: 1) a slight reduction of its ageostrophic part F_eK_{ea} (3%; Fig. 3), which is explained by changes in Ekman-induced surface current, and 2) a sink of energy through its geostrophic part F_eK_{eg} (actual negative values of F_eK_{eg}). In that sense, the current feedback acts as an "eddy killer." Figure 5 illustrates the geostrophic sink through F_eK_{eg} for an anticyclonic eddy with a southward uniform wind blowing up over such an eddy. In EXP1, over such an eddy, F_eK_{eg} is equal to zero.
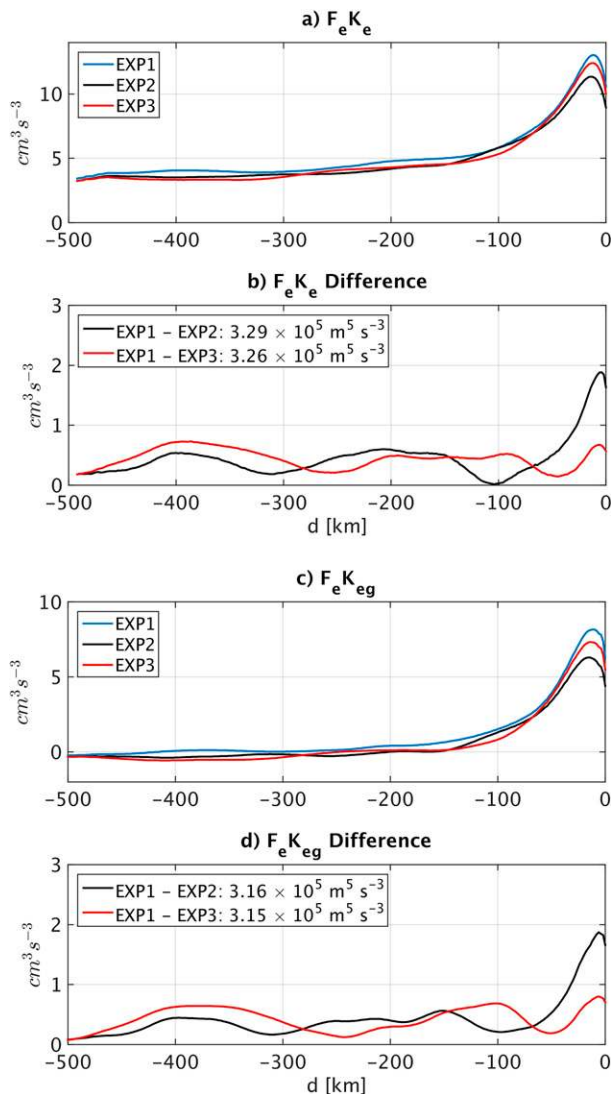
FIG. 3. (a) The F_eK_e cross-shore profiles (cm^3 s^{-3}) averaged between 30° and 45°N from EXP1 (blue), EXP2 (black), and EXP3 (red). (b) Differences between EXP1 and EXP2 (black) and EXP1 and EXP3 (red). (c) As in (a), but for F_eK_{eg}. (d) As in (b), but for the geostrophic eddy wind work F_eK_{eg}. The total integrated differences over the box (30°–45°N; $d = 500$ km) between EXP1 and the other experiments are indicated in the legend. Two regions can be distinguished: the coastal region (cross-shore distance $d <$ 80 km) and the offshore region ($d > 80$ km). In the coastal region, there is a reduction of F_eK_e mainly through its geostrophic component; in the offshore region, there is an actual sink of F_eK_e again through its geostrophic component F_eK_{eg}. The wind response to the current dampens the F_eK_e reduction.

Indeed, there is a positive F_eK_{eg} on the eastern branch and a negative F_eK_{eg} on the western branch, with a uniform wind; the net F_eK_{eg} is zero. In EXP2 the wind is still uniform in that it does not react to the current feedback. However, the eastern branch has currents moving in the same direction as the wind and hence has a

reduced surface stress, $\tau = C_d\rho_a(U_a - U_o)^2 < C_d\rho_a(U_a)^2$ (C_d is the drag coefficient). The western branch has currents moving against the wind, and hence has an increased surface stress, $\tau = C_d\rho_a(U_a - U_o)^2 > C_d\rho_a(U_a)^2$. As a result, the positive (negative) part of F_eK_{eg} is reduced (increased), and the net F_eK_{eg} becomes negative, deflecting energy from the ocean to the atmosphere. In EXP3, the current feedback not only acts on the surface stress but also on the atmosphere and, in particular, on the wind. Because of local changes in the surface stress, the wind can locally accelerate or decelerate. The wind response dampens the efficiency of the F_eK_{eg} sink, explaining the dampening of the offshore EKE reduction from EXP2 to EXP3 shown in Fig. 1. Indeed, on the eastern branch of the eddy, there is less friction, and the wind can accelerate, increasing the relative wind and hence increasing F_eK_{eg}. On the western branch, there is more friction, which leads to a decrease in the wind and hence to a less negative F_eK_{eg}. The net F_eK_{eg} in EXP3 is still negative but less than EXP2; the atmospheric response tends to reenergize the ocean.

In the coastal band 80 km in width, there is a reduction of energy input through F_eK_{eg}. As for the offshore region, the presence of eddies weakens the wind work. However, the wind perturbations induce an oceanic geostrophic coastal jet that blows partially in the same direction as the wind. Hence, the relative wind $U = U_a - U_o$ taken into account to estimate the surface stress in EXP2 and EXP3 is weaker than the absolute wind U_a used in EXP1 to estimate the stress. As a result, the stress perturbations are reduced in EXP2 and EXP3 in respect to EXP1, thus reducing F_eK_{eg} (Fig. 6). In EXP3, as for the offshore region, the atmospheric response dampens the current-induced surface stress reduction by changing the wind (Figs. 5 and 6).

To sum up, although the atmospheric response tends to reenergize the ocean, the current feedback to the atmosphere acts as an eddy killer and induces an energy sink from the ocean to the atmosphere. Although the F_eK_e sink of energy should be less effective in EXP3 compared to EXP2, Fig. 3 shows that the offshore F_eK_{eg} in EXP3 is only slightly larger than the one in EXP2. In EXP3, more EKE is generated in the coastal region; it then propagates offshore. As a result, there is a larger offshore energetic reservoir and therefore a larger F_eK_{eg} sink.

A cospectrum analysis of the total wind work FK and its geostrophic part (FK$_g$) is performed pointwise for the coastal (30°–45°N; $d \leq 80$ km) and offshore regions (30°–45°N; $d > 80$ km) (Fig. 7).

Both F_eK_e and F_eK_{eg} show large positive energy input at the low end of the frequency range, which mostly represent the annual cycle of winds acting on the mean California Current and surface Ekman velocity. The focus of this study is fairly tiny perturbations from this dominant process that induce a dampening of the EKE.
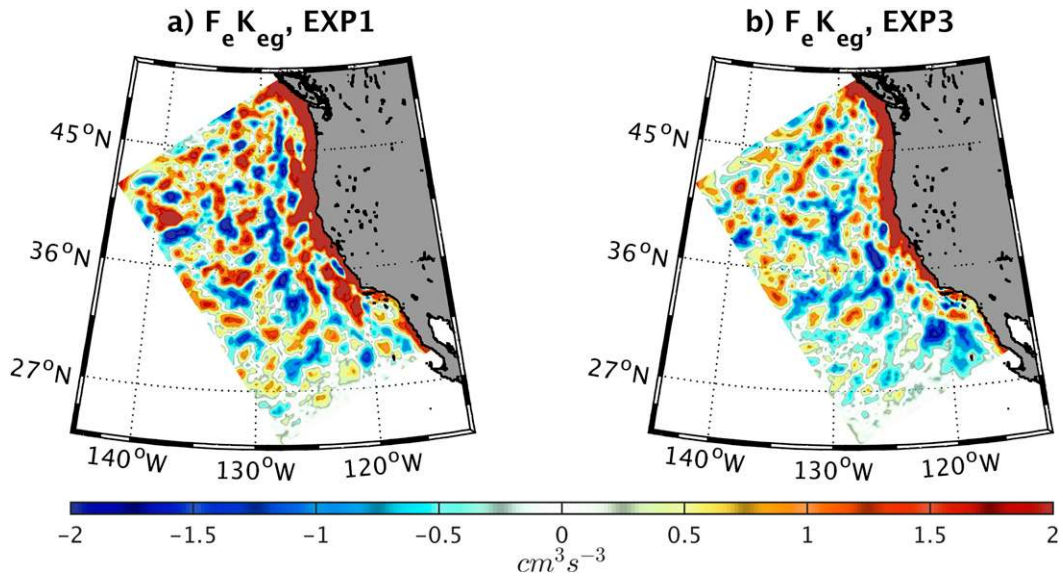
FIG. 4. Geostrophic eddy wind work $F_e K_{eg}$ from (a) EXP1 and (b) EXP3. The reduction of $F_e K_e$ is mainly explained by a coastal reduction of $F_e K_{eg}$ and an offshore sink of energy through $F_e K_{eg}$.

Consistent with the previous results, in the coastal region the current feedback to the surface stress reduces the amount of energy input into the ocean between the frequencies $30\,\mathrm{day}^{-1}$ and $300\,\mathrm{day}^{-1}$ (not shown). More interestingly, as illustrated in Fig. 7 using EXP1 and EXP3, offshore between $30\,\mathrm{day}^{-1}$ and $300\,\mathrm{day}^{-1}$, there is a clear FK reduction due to a sink of FK_g, this leads to a transfer of energy from the ocean to the atmosphere. The sink of energy from the geostrophic currents to the atmosphere within the eddy scale band confirms that the current feedback acts as an eddy killer. As a consequence, the eddies decay as they propagate offshore and are therefore eventually quite weak (or absent) very far offshore, explaining the offshore decay of EKE in Fig. 1. Thus, there is a route of energy from the atmosphere to the ocean in the nearshore region, an offshore eddy propagation, and then a route from the offshore eddies to the atmosphere. Finally, in our analysis the seasonal variability is not removed. At seasonal time scale, the wind has roughly the same direction as the surface currents so that there is a seasonal positive geostrophic $F_e K_e$. The same analysis done without the seasonal variability leads qualitatively to the same results but with a slightly larger negative $F_e K_{eg}$ offshore (by 5%). The large values of positive $F_e K_e$ in the nearshore region are also partly driven by the seasonal variability that represents about 30% of the coastal positive $F_e K_e$ (about 30%).

4. Surface stress and wind response

As reported by Chelton et al. (2007), the link between SST and wind stress in the California upwelling system exhibits a linear relationship between the wind stress curl and the crosswind SST gradient. EXP1 has a wind stress curl–crosswind SST gradient slope of $s_t = 0.019\,\mathrm{N\,m}^{-2}\,{}^{\circ}\mathrm{C}^{-1}$ for the summer season that is similar to the one reported by Chelton et al. (2007). Similar values are found in the other experiments. Here the focus is on an analogous linear relationship between the surface stress and the oceanic currents and on the influence of surface currents on the surface wind speed, which apparently has not previously been documented.

a. Current-induced surface stress

Similar to Chelton et al. (2007), the statistical relationship between surface stress curl and oceanic current vorticity is evaluated by bin averaging the 1-month running means of the stress curl as a function of the 1-month running means of the oceanic current vorticity over the full simulated period for the three experiments. Bin sizes of $1\,\mathrm{m\,s}^{-1}\,(100\,\mathrm{km})^{-1}$ and $1\,\mathrm{N\,m}^{-2}$ $(10^5\,\mathrm{km})^{-1}$ are used for surface current vorticity and the stress curl, respectively. The large-scale signal is removed using a high-pass Gaussian spatial filter with a 150 km cutoff. The analysis domain is 30°–45°N and $(150 < d < 500\,\mathrm{km})$: that is, offshore of the wind drop-off region where the current feedback effects are partly masked by the orographic, coastline, and SST effects on the wind (Perlin et al. 2011; Renault et al. 2015).

Figure 8 shows the resulting scatterplots. A coupling correlation coefficient s_{st} ($\mathrm{N\,s\,m}^{-3}$), where the subscript "st" represents stress, is defined as the slope of the linear regression in this scatterplot. Because EXP1 does not consider the surface currents in its surface stress
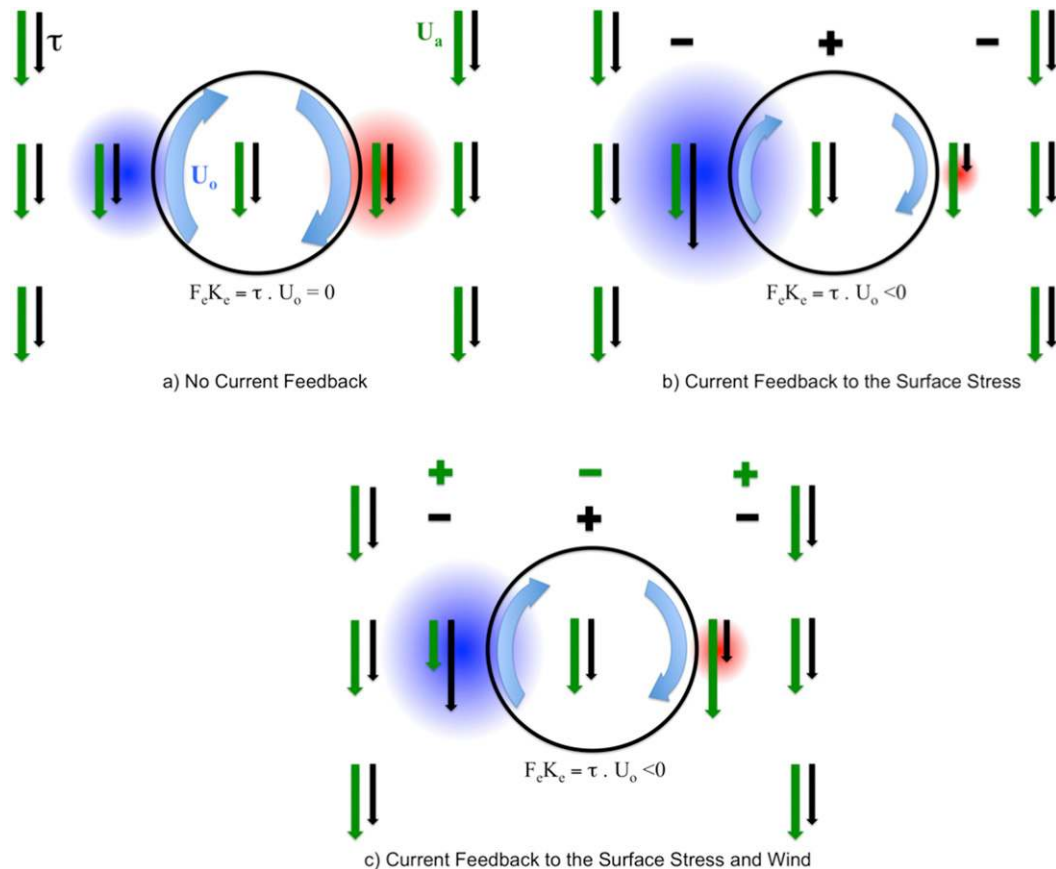
FIG. 5. Schematic representation of the current feedback effects over an anticyclonic eddy, considering a uniform southward wind. The arrows represent the wind (green), surface stress (black), and surface current (blue). The red (blue) shade indicates a positive (negative) F_eK_e. The black (green) $+/-$ signs indicate the current-induced stress (wind) curl. (a) A simulation without current feedback (e.g., EXP1). (b) A simulation that takes into account the current feedback in the estimation of the surface stress but neglects the atmospheric response (e.g., EXP2). And (c) a fully coupled simulation that has the current feedback in the surface stress estimate and the atmospheric response (e.g., EXP3). In EXP1 (i.e., simulations without current feedback), the net F_eK_e is equal to zero. In EXP2 (i.e., simulations with current feedback to the surface stress), over an eddy, the amount of positive wind work F_eK_e is reduced, and the amount of negative F_eK_e becomes more negative. As a result, the net F_eK_e becomes negative, deflecting energy out of the eddy into the atmosphere. In a fully coupled model (EXP3), the atmospheric response dampens the sink of F_eK_e by increasing the positive F_eK_e and decreasing the negative F_eK_e; the net F_eK_e remains negative. The current feedback induces a positive (negative) stress curl (wind curl) in the eddy's center.

estimate, its wind stress curl does not show any significant dependence on the oceanic vorticity. EXP2 and EXP3 show a clear negative linear relationship between the surface currents vorticity and the surface stress curl, with $s_{st} < 0$. The negative sign is consistent with the F_eK_{eg} sink and Fig. 5: that is, the current feedback induces an opposite sign surface stress curl. From EXP2 to EXP3, the magnitude of s_{st} decreases significantly. The difference is due to the atmospheric response of an intensification of the surface wind that attenuates the current feedback effect on the surface stress. Simulations that neglect the wind adjustment to the current feedback [e.g., EXP2 and the North Atlantic simulations of Eden and Dietze (2009)] overestimate the reduction

of the surface stress by the oceanic surface currents, missing the partial reenergization of both the atmosphere and ocean through full coupling.

b. Wind response

The oceanic surface currents partially drive the atmosphere. When coupling the atmosphere to the oceanic currents, the reduction in air–sea velocity difference reduces the stress acting on the wind and allows it to accelerate. Figure 9 depicts the mean cross-shore profiles of surface wind turbulent kinetic energy (TKE) at 30°N and 45°N. TKE is always larger in EXP3 than in EXP1, which reflects the changes in surface stress. Interestingly, the nearshore region ($d \leq 80$ km) has a higher TKE
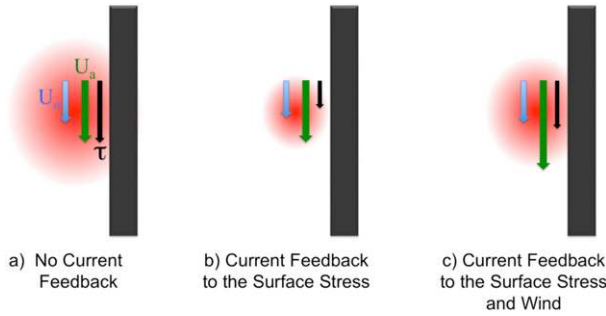
FIG. 6. Schematic representation of the current feedback considering a uniform southward wind blowing along the coast. (a) A simulation without current feedback (e.g., EXP1). (b) A simulation that takes into account the current feedback in the estimation of the surface stress but neglects the atmospheric response (e.g., EXP2). And (c) a fully coupled simulation: that is, one that has the current feedback into the stress estimate and the atmospheric response (e.g., EXP3). The arrows represent the wind (green), surface stress (black), and oceanic surface current (blue). The red shade represents the induced $F_e K_e$ (positive in all cases). The wind induces an oceanic coastal geostrophic jet that is partially in the same direction as the wind, inducing a positive $F_e K_e$. From EXP1 to EXP2, the reduction of the stress induces, in turn, a weakening of $F_e K_e$. From EXP2 to EXP3, the wind accelerates, increasing the surface stress and hence $F_e K_e$ and the oceanic coastal geostrophic jet.

difference than the offshore region. This is likely partly explained by the presence of the steady oceanic geostrophic jet that flows in the same direction as the wind, reducing the surface stress near the coast.

Binned scatterplots of 1-month running means of wind curl and surface current vorticity over the domain 30°–45°N and (150 < d < 500 km) are calculated for EXP1 and EXP3. EXP1, as expected, does not have any significant relationship between wind curl and surface current vorticity (not shown). EXP3 has a clear linear relationship between them (Fig. 10a). A nondimensional coupling coefficient s_w is defined from the slope of the linear regression estimated from the scatterplot. The positive s_w indicates a positive forcing of the currents on the wind, a positive (negative) current vorticity inducing a positive (negative) wind curl. The wind changes are explained by the surface stress changes: a weaker surface stress allows the wind to accelerate. The coefficient s_w counteracts the effect expressed in s_{st} and hence acts to reduce s_{st} from EXP2 to EXP3. The positive s_w is also consistent with Fig. 5, the currents inducing a positive wind curl in the center of an anticyclonic eddy, which counteracts the current-induced negative surface stress curl. Figure 10b depicts the vertical structure of the coupling coefficient s_w. The current feedback mainly shapes the surface wind; however, its effect can be felt up to 300 m. Finally, a spectral analysis reveals the current feedback mainly affects the wind at eddy scale (but can be felt slightly over several hundreds
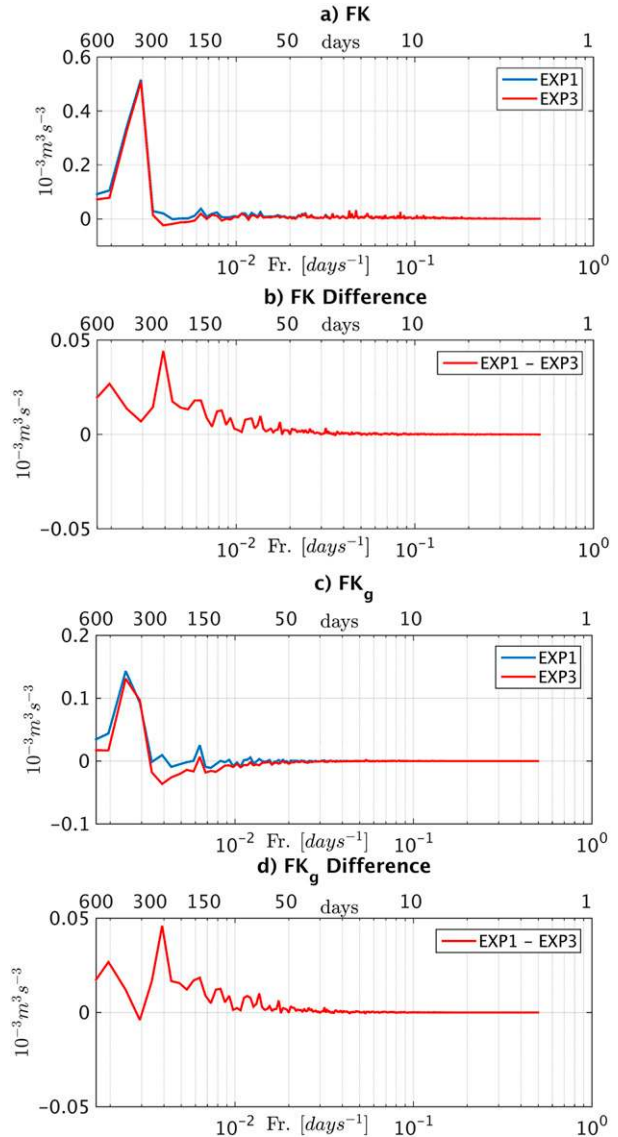

FIG. 7. (a) Temporal 1D cospectrum of the total wind work FK from EXP1 and EXP3 between 30° and 45°N for the offshore region ($d > 80$ km). (b) Difference between EXP1 and EXP3. (c),(d) As in (a),(b), but for the geostrophic wind work. The current feedback to the atmosphere acts as an eddy killer by reducing $F_e K_e$ through its geostrophic component, deflecting energy from the ocean to the atmosphere.

of kilometers) and over the time scale between 30 and 300 days^{-1} (not shown). To our knowledge this is an entirely new phenomenon that has not previously been pointed out. Finally, although the wind changes have an important effect on the oceanic response, from the atmospheric point of view the changes are rather small. The planetary boundary layer height is not changed, nor are the mean overlying circulation, clouds, or precipitation. For more dynamical regions, we expect a larger large-scale effect.
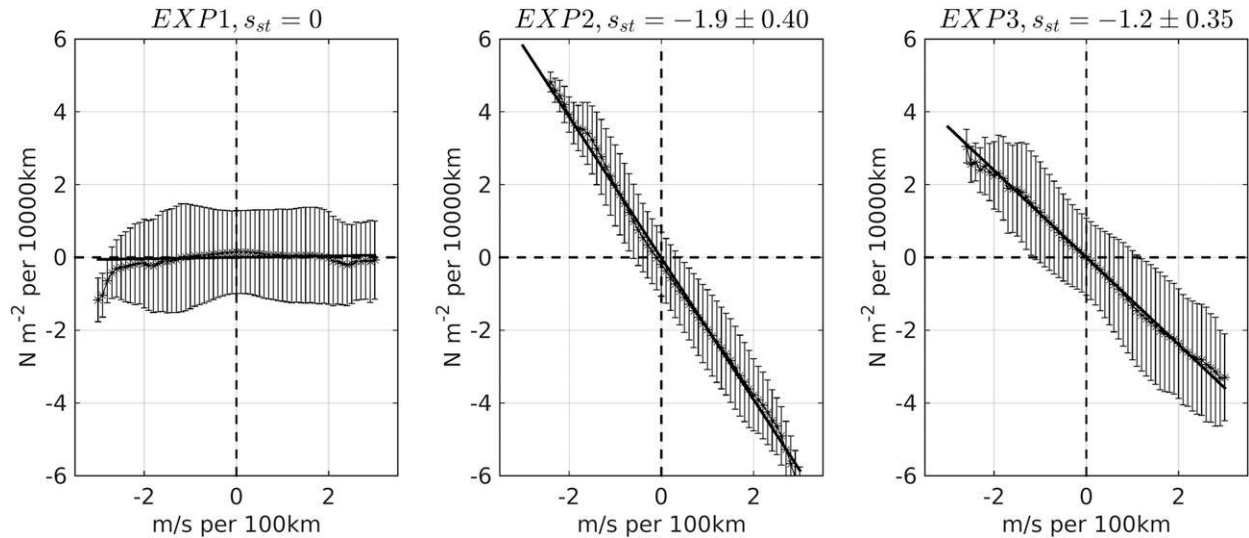
FIG. 8. Binned scatterplot of the full time series of 1-month running means of surface stress curl and surface current vorticity over the domain 30°–45°N and ($150 < d < 500$ km). The bars indicate plus and minus one the standard deviation about the average drawn by stars. The linear regression is indicated by a black line, and the slope s_{st} is indicated in the title (10^{-2} N s m^{-3}). (left)–(right) EXP1, EXP2, and EXP3. EXP1 does not have a significant slope because it does not have the current feedback to the atmosphere, nor the surface stress. EXP2 and EXP3 present a clear negative linear relationship between currents and stress curl. The current feedback induces finescale wind stress structure. Consistent with the previous results, the atmospheric response reduces the current feedback effect on the stress.

5. Induced Ekman pumping and eddy attenuation time

By shaping the surface stress, the current feedback to the atmosphere induces an additional Ekman pumping in the ocean that provides a mechanism for weakening an eddy (i.e., the eddy dampening by the current feedback). Note that Seo et al. (2016) for the U.S. West Coast show the SST feedback induces comparable Ekman pumping velocity as the current feedback. However, it primarily affects the eddy propagation, with no effect on the amplitude. This is consistent with Gaube et al. (2015), who show using observations that the SST-induced Ekman pumping is generally a secondary effect for offshore eddies. The Ekman pumping is

$$w_{ek} = \mathbf{k} \cdot \nabla \times \frac{\boldsymbol{\tau}}{\rho_0 f}, \tag{12}$$

where f is the Coriolis frequency. Using the current coupling coefficient s_{st} from EXP3, (12) becomes

$$w_{ek} = \frac{s_{st}\Omega_{surf}}{\rho_0 f}, \tag{13}$$

where the surface current vorticity is $\Omega_{surf} = \mathbf{k}$. Using (12) and a typical $\Omega_{surf} = 1 \times 10^{-5}$ s^{-1} on a scale of 100 km, $w_{ek} = 10$ cm day^{-1}, which is similar to the estimate in Gaube et al. (2015).

An attenuation time scale of eddies is then estimated as a result of the current-induced surface stress curl and, to

check the results from an energetic point of view, of the sink of $F_e K_e$. In a similar way to that described by Gaube et al. (2015), the decay time scale of an eddy associated with the stress curl can be estimated from a simplified vertically integrated barotropic vorticity balance:

$$\frac{\partial \Omega_{bt}}{\partial t} = \mathbf{k} \cdot \nabla_c \times \frac{\boldsymbol{\tau}}{\rho_0}, \tag{14}$$
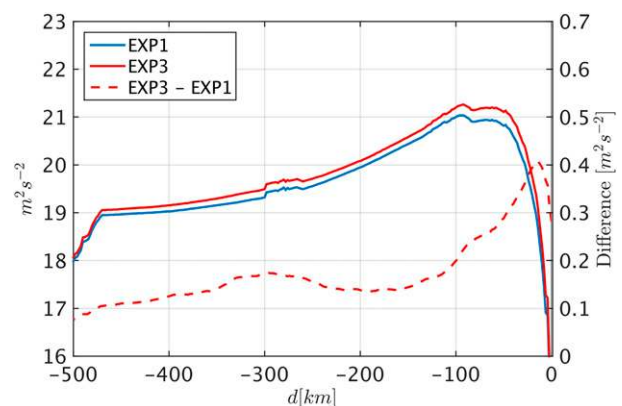

FIG. 9. Cross-shore profile of the TKE of the surface wind averaged between 30° and 45°N from EXP1 (cyan) and EXP3 (red). The $F_e K_e$ sink from the ocean to the atmosphere results in a slightly larger TKE in EXP3 compared to EXP1. In the nearshore region, there is a larger wind enhancement that is likely partly explained by the presence of the steady oceanic geostrophic jet that flows in the same direction as the wind.
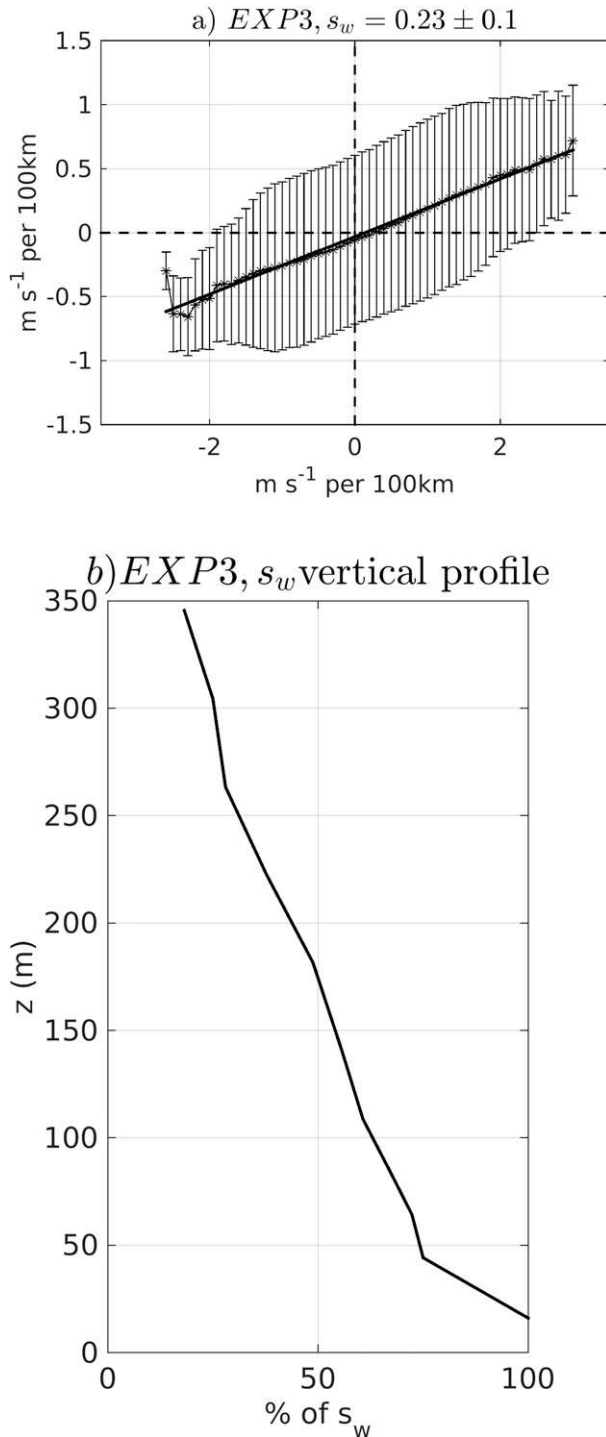
FIG. 10. (a) As in Fig. 8, but for the wind curl and the surface current vorticity in EXP3. There is a positive linear relationship between the current vorticity and the wind curl (i.e., the current feedback on the atmosphere induces finescale structures in the wind field that counteract the current-induced stress structure) (Fig. 8). This explains the dampening of the current feedback effect on the EKE. The linear regression is indicated by a black line, and the dimensionless slope s_w is indicated in the title. (b) Vertical attenuation of s_w with respect to the surface s_w.

where the eddy barotropic vorticity is defined as the vorticity of the integrated velocities,

$$\Omega_{bt} = \frac{\partial \overline{v}^z}{\partial x} - \frac{\partial \overline{u}^z}{\partial y}. \qquad (15)$$

The surface stress curl induced by the current feedback is $\nabla_c \times \boldsymbol{\tau}$, and $\overline{u}^z$ and $\overline{v}^z$ are the zonal and meridional mean depth-integrated current components.

Figure 11 shows a snapshot of the surface current vorticity and a 2000-m vertically integrated current vorticity from EXP3. The integration is not to the bottom so as to be able to neglect the bottom drag effect on the eddies. At the surface there are small-scale features such as filaments that are not present in the depth integral; however, the main eddies can be seen from both the surface vorticity and the depth-integrated vorticity. The depth-integrated vorticity is about 500 larger than the surface vorticity. Therefore, a characteristic vertical scale of eddies $d = 500$ m can be estimated as a translation between the surface and depth-integrated vorticity:

$$\Omega_{bt} = D\Omega_{surf}. \qquad (16)$$

Using (16) and the current coupling coefficient s_{st}, (14) becomes identical to (14) of Gaube et al. (2015):

$$\frac{\partial \overline{\Omega}}{\partial t} = -\frac{f}{D} w_{ek}. \qquad (17)$$

Because the Ekman pumping induced by the current feedback has approximately the same horizontal shape as the eddy vorticity $(\overline{\Omega})$, this relation implies an eddy decay process, analogous to the spin down of a vortex above a solid boundary induced by a viscous Ekman layer.

An eddy attenuation time scale can be estimated from a simplified vorticity budget [(17)] as

$$t_{vrt} = \frac{\rho_0 D}{s_{st}}. \qquad (18)$$

As previously noted by Gaube et al. (2015), this estimate of eddy attenuation time depends only on D, and in this study, the current coupling coefficient s_{st}, not the eddy amplitude or radius. Note that s_{st} depends on the background wind, which for the CCS is about $5\,\mathrm{m\,s}^{-1}$. For an eddy with $D = 500$ m under a uniform background wind of $5\,\mathrm{m\,s}^{-1}$ and using s_{st} from EXP2 ($s_{st} = 0\,019\,\mathrm{N\,s\,m}^{-3}$) or from EXP3 ($s_{st} = 0\,012\,\mathrm{N\,s\,m}^{-3}$), the eddy attenuation time is $t_{vrt} = 313$ or 495 days, respectively. Not surprisingly, when the atmospheric adjustment is neglected, the eddy attenuation time scale is underestimated. Given (18), the shallower the mesoscale eddy is, the shorter the eddy attenuation time is.
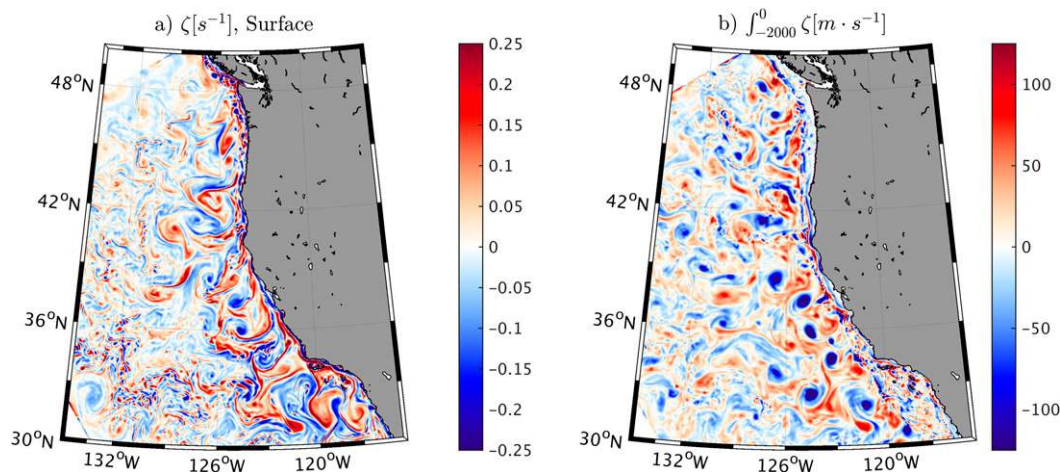
FIG. 11. (a) Snapshot of the sea surface relative vorticity. (b) The 2000-m integrated relative vorticity, from EXP3. The color-bar scale is adjusted between (a) and (b) by a factor of $D = 500$, which allows a rough match between (a) and (b). The factor D is interpreted as the characteristic vertical scale of the eddies.

This eddy attenuation time t_{vrt} can be directly compared to the one estimated from the observations by Gaube et al. (2015). From (19) in Gaube et al. (2015), the wind background here and a surface drag coefficient of $C_d = 0.012$ (Large and Pond 1981), the eddy attenuation time scale is 541 days, which is close to the t_{vrt} in EXP3 (i.e., by taking into account the atmospheric adjustment to the current feedback). An eddy attenuation time scale can also be estimated from an energy perspective; in that case, because of the quadratic form of the EKE, such a time scale is equal to $t_{vrt}/2$ (roughly 250 days for EXP3 and 156 days for EXP2).

In EXP3, the current feedback reduces the surface EKE by 44% (Fig. 1). However, it only reduces the total integrated EKE by 27%. This is explained by the eddy attenuation time scale that depends on the depth scale of the eddies and on the depth structure of the eddy response. The shallower the eddies are, the more sensitive they are to the current feedback. An alternative interpretation is that the wind dampening at the surface changes the vertical structure of the eddies over their lifetime (with the initial structure being set by the baroclinic instability that generates them, generally something close to the first baroclinic mode). The anticyclonic eddy observed by (McGillicuddy et al. 2007) and the cyclonic "thinny" described in a recent paper (McGillicuddy 2015) may be examples of this.

6. Eddy statistics

The eddy tracking method (section 2f) was applied to EXP1, EXP3, and AVISO. Overall, the simulations show a fair agreement with the observations and

previous analyses (Chelton et al. 2011; Kurian et al. 2011). Figure 12 shows the eddy sea surface height (SSH) amplitude and rotational speed distributions. The simulation EXP1 without the current feedback overestimates the eddy SSH and rotational speed compared to the observations. It also underestimates the eddy scale and overestimates the eddy life (not shown), allowing the eddies to propagate further offshore. This is consistent with the too-large offshore EKE in EXP1 (Fig. 1). Because of a reduction of the eddy amplitude, rotational speed, and eddy life (not shown), EXP3 presents a better agreement with the AVISO results through the eddy killing mechanism.

Recently, Samelson et al. (2014) showed a composite life cycle for a long-lived mesoscale eddy: on average, the eddy first grows in SSH amplitude, then has a slow growth followed by a slow symmetric decay, and, at the end, the eddy amplitude decreases rapidly before collapsing (see, for example, Fig. 2 of Samelson et al. 2014). They show a stochastic model was able to predict accurately the eddy life symmetry and thus suggest that the evolution of mesoscale structures is dominated by effective stochastic interactions, rather than by the classical wave mean cycle of initial growth followed by nonlinear equilibration and barotropic, radiative, or frictional decay, or by the vortex merger processes of inverse turbulent cascade theory. The lengthy stabilization of the composite eddy and its property of symmetry between its growing and decay phases contradicts the results in Gaube et al. (2015) and our own. The eddy should rapidly intensify as it forms; it then eventually has slow growth, but it should decay in an asymmetric way because of the current
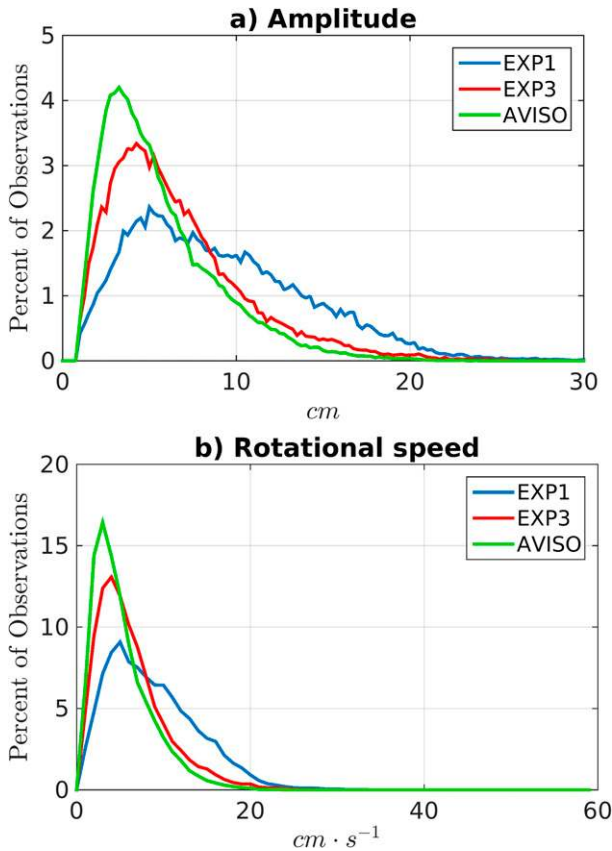
FIG. 12. Long-lived (16 weeks) eddy (a) amplitude and (b) rotational speed statistics from EXP1 (blue), EXP3 (red), and AVISO (green). Consistent with the previous results, the current feedback to the atmosphere dampens the eddy amplitude and rotational speed, improving the realism of the simulation.

feedback eddy dampening. Figure 13 shows the evolution of the normalized amplitude $\mathcal{A}$ as a function of the normalized time $\mathcal{T}$ for all tracked eddies with a lifetime greater than 16 weeks (cf. Fig. 2 in Samelson et al. 2014). As in Samelson et al. (2014), each eddy amplitude time series was normalized by its time mean, and the respective lifetime $\mathcal{L}$ by using the convention $\mathcal{T}1 = 1/2J$ and $\mathcal{TL} = 1 - (1/2J)$, J being the length of the time series. In both EXP3 and AVISO, the eddy first grows in strength, then decreases slowly (by 10%) from $\mathcal{T} = 0.3$ to $\mathcal{T} = 0.7$, and finally, decreases rapidly before collapsing (presumably through some destructive interaction with other currents). This supports the current-induced eddy killing as a realistic mechanism. In EXP1, the systematic eddy decay during its middle phase seems to be absent. The decay time scale of an eddy associated with the current feedback is also estimated using Fig. 13. During the slow decay present in EXP3 (and not in EXP1), the eddy amplitude is reduced by 10% in roughly $0.4\mathcal{L}$.
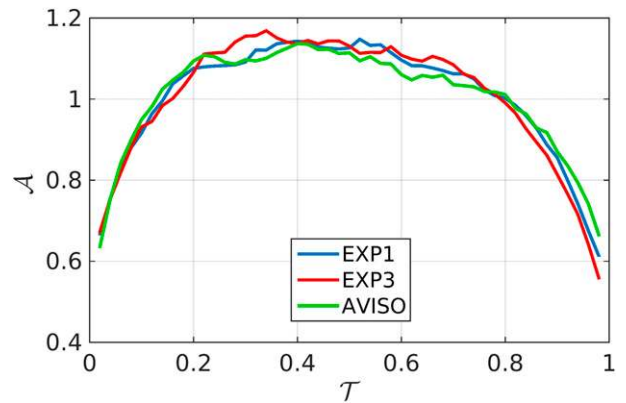

FIG. 13. Evolution of eddy normalized amplitude $\mathcal{A}$ as a function of their dimensionless time $\mathcal{T}$ for all tracked eddies with a lifetime greater than 16 weeks. The blue, red, and green colors represent the results from EXP1, EXP3, and AVISO. In EXP3, consistent with AVISO, the eddy first grows in size, then, because of the current feedback to the atmosphere, decreases slowly, and finally, decreases rapidly before collapsing. In EXP1, the slow decrease is not evident.

Using a long-lived eddy mean life of 206 days, a decay time scale t_{eddy} of 527 days is estimated and is consistent with the previous estimation of t_{vrt} and the Gaube et al. (2015) estimate. The discrepancies with the Samelson et al. (2014) results will need further investigation.

Figures 12 and 13 do show some discrepancies between EXP3 and AVISO. While no doubt some of these are due to model bias, there are important sampling differences. In particular, the AVISO data have spatial and temporal resolution issues and see only the larger mesoscale eddies (Chelton et al. 2011).

7. Discussion and conclusions

Using coupled ocean–atmosphere simulations, we assess the role of the current feedback through the surface wind work, the energy transfer from the atmosphere to the ocean, and its consequences for both oceanic and atmospheric mesoscale activity. In good agreement with former studies, we show the current feedback strongly attenuates the oceanic EKE. A simplified EKE budget shows the current feedback acts on the eddy wind work F_eK_e through its geostrophic component. In the coastal region, it reduces the energy transfer from the atmosphere to the ocean, while offshore it induces a deflection of the energy from the oceanic geostrophic currents (eddies) to the atmosphere. As a result, there is less coastal generation of EKE and dampening or even killing of eddies offshore.

The current feedback can be split into two actions: 1) on the surface stress and 2) on the wind. The action on

the stress induces the EKE dampening by reducing the energy transfer from the atmosphere to the ocean and even reversing it through the offshore geostrophic currents. For the U.S. West Coast, we determine the coupling coefficients between the oceanic surface current and the surface stress, and between the oceanic surface current and the wind, which are opposing effects. The current feedback has a negative action on the surface stress, a positive (negative) surface vorticity inducing a negative (positive) stress curl. For the first time, we show the wind response to the current feedback partly counteracts the stress effect and therefore partly reenergizes the ocean. In the nearshore region, as a result of less transfer of energy from the atmosphere to the ocean, the wind accelerates, increasing the nearshore surface stress and hence the coastal EKE generation. Offshore, there is a positive feedback: a positive surface vorticity inducing a positive wind curl (leading to a positive coupling coefficient), dampening the negative current-induced surface stress curl. A simulation that neglects the atmospheric adjustment to the reduced stress [as EXP2 or Eden and Dietze (2009)] systematically overestimates the attenuation of the EKE. There is a route of energy from the atmosphere into the nearshore ocean, offshore energy propagation in the ocean, and then from the offshore ocean to the atmosphere.

Using the current–wind stress coupling coefficient, an eddy attenuation time scale is estimated from a vorticity balance perspective. As shown previously by Gaube et al. (2015), the derived eddy attenuation time scale depends on the characteristic vertical scale of the eddies D and the current coupling coefficient s_{st} (which depends on the background wind). Using mean parameters for the CCS, we estimate an eddy attenuation time scale of $t_{vrt} = 495$ days that is consistent with the estimate in Gaube et al. (2015). A simulation that neglects the atmospheric adjustment to the current feedback underestimates the eddy attenuation time scale ($t_{vrt} = 313$ days in EXP2). We show a similar time scale can be estimated during the slow decay period of the composite average life cycle of long-lived eddies.

Gaube et al. (2015) provides a satellite-based validation of our results. A more direct validation is made here using eddy statistics applied on the coupled simulation without current feedback (i.e., EXP1) and applied on a fully coupled simulation (i.e., EXP3). Consistent with a reduction of the EKE, the coastal reduction of the energy transfer from the atmosphere to the ocean and the sink of energy from the offshore ocean to the atmosphere actually reduces the eddies' amplitudes and rotational speeds in a realistic way. Simulations that resolve the EKE without current feedback (i.e., forced by prescribed wind stress or a bulk formula without

current feedback) may systematically overestimate the EKE. We also show that the current feedback to the atmosphere also reduces the eddy lifetime in EXP3 and is consistent with the observed composite life cycle of rapid early intensification, a prolonged middle stage of slow decay due to eddy killing by the current feedback, and an abrupt collapse at the end.

A regional high-resolution atmospheric model is usually very costly compared to an oceanic model. So an important next question is how best to force an uncoupled oceanic model. A simulation that uses prescribed wind stress cannot dampen the offshore eddies because the prescribed wind stress is correlated with the eddies. A bulk-forced oceanic simulation (i.e., where the model is forced by the wind) should estimate the surface stress using the relative wind. A distinction is necessary between observations or a fully coupled model, on one hand, and an uncoupled atmospheric wind product, on the other. For nondeterministic variability (such as oceanic eddies), the bulk formulae used to estimate the surface stress should, in any case, take into account a parameterization of the partial reenergization of the ocean by the atmospheric response. The surface stress could be estimated with a velocity that is the wind relative to the current corrected by the current–wind coupling coefficient s_w:

$$U = U_a - (1 - s_w)U_o. \qquad (19)$$

For the U.S. West Coast, $s_w = 0.23$ can be derived from Fig. 10. However, it remains to be seen how well this modified relative wind parameterization would work for an uncoupled model, and the current–wind coupling coefficient found in this study may not be valid for other regions, pending further investigation. The coupling coefficient depends on several local parameters, such as the background wind, the steadiness, and the EKE. Even for the CCS, the wind coupling coefficient may not be accurate for the nearshore region; there the wind adjustment is stronger, canceling more efficiently the reduction of energy transfer from the atmosphere to the ocean. For deterministic features, such an adjustment may not be necessary if the model is forced by observations or some adequate representation of the oceanic currents. For instance, for a U.S. West Coast configuration forced by the QuikSCAT wind stress observations (e.g., Capet et al. 2008a; Renault et al. 2016). the simulated wind-driven alongshore current perturbations may be correlated to the climatological average currents and hence already contain both the atmospheric adjustment to the current feedback and the reduction of the surface stress perturbations, allowing a realistic EKE close to the coast. However, the eddies generated

are not correlated with the reality lying behind the measured stress, so such simulations cannot represent the offshore sink of energy from the ocean to the atmosphere, explaining their offshore EKE overestimation. Finally, for low-resolution simulations (e.g., global circulation models), because the EKE is already underestimated, taking into account the current feedback to the atmosphere would induce a larger EKE underestimation, degrading the realism of the simulation.

The current effect on the wind speed should be assessed from the observations. A scatterometer (such as QuikSCAT) is fundamentally a stress measuring instrument. The winds are reported as so-called equivalent neutral stability winds, which is the wind that would exist if the conditions were neutrally stable and the ocean current were zero. Therefore, it is not possible to determine from scatterometry alone what the actual surface wind is. Dedicated studies using scatterometer and other observations (e.g., in situ ones) should aim to address this issue.

In this study of the CCS, although the perturbations are clearly modulated by the current feedback, the mean surface stress and current are not significantly changed. However, they may be impacted in other regions with stronger currents and/or stronger SST fronts, such as the Gulf Stream area. An expanded Lorenz diagram of the depth-integrated energy budget (Lorenz 1955) for the ocean could include a sink of energy by negative geostrophic wind work induced by the current feedback. Consistent with Wang and Huang (2004), the total F_eK_e is much larger than its geostrophic component F_eK_{eg}. Substantial power goes into the surface Ekman currents (Wang and Huang 2004), and much of this is dissipated within the upper few tens of meters (i.e., in the Ekman layer); therefore, it is not available to drive currents and diapycnal mixing deeper in the water column. Two strong pathways of mechanical energy from the surface to the deeper ocean are clear at present: wind forcing of near-inertial oscillations and wind forcing of surface Ekman currents and geostrophic flow (Alford 2003; Watanabe and Hibiya 2002; Scott and Xu 2009). In EXP3, F_eK_e integrated over the whole domain is an energy conversion of $16.9 \times 10^6 \, \mathrm{m^5 \, s^{-3}}$, whereas F_eK_{eg} is only $2.1 \times 10^6 \, \mathrm{m^5 \, s^{-3}}$. We show the current feedback to the atmosphere mainly acts through the latter. Figure 14 expands the Lorentz diagram of energy conversion for the depth-integrated EKE, integrated over the whole U.S. West Coast domain during the 1995–99 period. It includes the geostrophic wind work F_eK_{eg} and the baroclinic (P_eK_e) and barotropic conversions (K_mK_e). Several energy conversion arrows are added: the current-induced eddy geostrophic wind work, $F_eK_{egc} = F_eK_{eg\_EXP1} - F_eK_{eg\_EXP3}$, the current-induced baroclinic
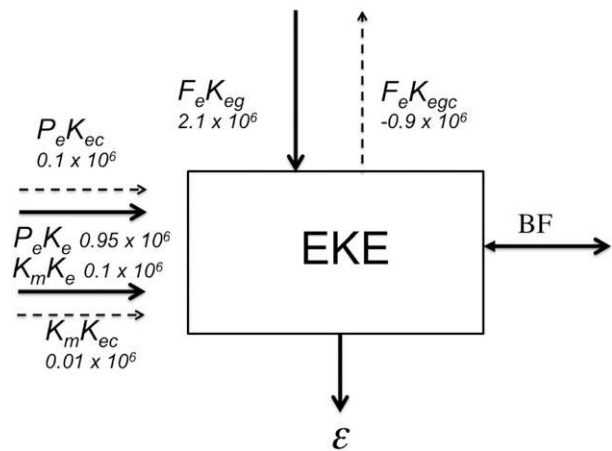

FIG. 14. An expanded Lorenz diagram of energy conversion ($\mathrm{m^5 \, s^{-3}}$) for the depth-integrated EKE, integrated over the whole U.S. West Coast domain for the period 1995–99. The atmosphere is above, and mean ocean KE and PE are to the left (not represented). The solid lines represent the classic energy conversion terms (i.e., F_eK_{eg}, P_eK_e, and K_mK_e), whereas the dashed lines depict new energy conversion terms induced by the current feedback (i.e., F_eK_{egc}, P_eK_{ec}, and K_mK_{ec}; see text). The current feedback to the atmosphere mainly removes energy from the ocean to the atmosphere through the geostrophic flow. The dissipation term is ϵ, and the energy flux through the boundary is BF. See text for more information.

conversion, $P_eK_{ec} = P_eK_{e\_EXP1} - P_eK_{e\_EXP3}$, and the current-induced barotropic conversion $K_mK_{ec} = K_mK_{e\_EXP1} - K_mK_{e\_EXP3}$. The geostrophic wind work F_eK_{egc} represents 29% of the total energy input (defined as the sum of F_eK_{eg}, P_eK_e, and K_mK_e) and 43% of F_eK_{eg}. The baroclinic and barotropic conversions adjust to slightly counteract the wind work reduction, inducing a positive power input of 3% of the total eddy energy input. The EKE input is then reduced by 26%, which roughly corresponds to the depth-integrated EKE reduction (27%).

In summary, ocean–atmosphere models should take into account the current feedback to have a realistic representation of the EKE and its associated processes. This might be even more important for biogeochemical models. In the open ocean, and in particular in low-nutrient environments, mesoscale processes increase the net upward flux of limiting nutrients and enhance biological production (Martin and Richards 2001; McGillicuddy et al. 2007; Gaube et al. 2013). McGillicuddy et al. (2007), using observations, show the effects of surface currents on Ekman pumping in eddies and, in particular, how it affects the biology. In the EBUS, the eddies modulate biological productivity by subducting nutrients out of the euphotic zone and advecting biogeochemical material offshore (Gruber et al. 2011; Nagai et al. 2015; Renault et al. 2016). A simulation without current feedback—by

overestimating the eddy amplitude, lifetime, and spatial range—may overestimate their quenching and offshore transport effects on the biogeochemical materials. We intend to investigate this soon.

REFERENCES

Alford, M. H., 2003: Improved global maps and 54-year history of wind-work on ocean inertial motions. *Geophys. Res. Lett.*, **30**, 1424, doi:10.1029/2002GL016614.

Beckmann, A., and D. B. Haidvogel, 1993: Numerical simulation of flow around a tall isolated seamount. Part I: Problem formulation and model accuracy. *J. Phys. Oceanogr.*, **23**, 1736–1753, doi:10.1175/1520-0485(1993)023<1736:NSOFAA>2.0.CO;2.

Capet, X., P. Marchesiello, and J. C. McWilliams, 2004: Upwelling response to coastal wind profiles. *Geophys. Res. Lett.*, **31**, L13311, doi:10.1029/2004GL020123.

——, F. Colas, P. Penven, P. Marchesiello, and J. C. McWilliams, 2008a: Eddies in eastern boundary subtropical upwelling systems. *Ocean Modeling in an Eddying Regime. Geophys. Monogr.*, Amer. Geophys. Union, 131–147, doi:10.1029/177GM10.

——, J. McWilliams, M. Molemaker, and A. Shchepetkin, 2008b: Mesoscale to submesoscale transition in the California Current System. Part I: Flow structure, eddy flux, and observational tests. *J. Phys. Oceanogr.*, **38**, 29–43, doi:10.1175/2007JPO3671.1.

Carr, M.-E., and E. J. Kearns, 2003: Production regimes in four Eastern Boundary Current systems. *Deep-Sea Res. II*, **50**, 3199–3221, doi:10.1016/j.dsr2.2003.07.015.

Carton, J. A., and B. S. Giese, 2008: A reanalysis of ocean climate using Simple Ocean Data Assimilation (SODA). *Mon. Wea. Rev.*, **136**, 2999–3017, doi:10.1175/2007MWR1978.1.

Chaigneau, A., M. Le Texier, G. Eldin, C. Grados, and O. Pizarro, 2011: Vertical structure of mesoscale eddies in the eastern South Pacific Ocean: A composite analysis from altimetry and Argo profiling floats. *J. Geophys. Res.*, **116**, C11025, doi:10.1029/2011JC007134.

Chelton, D. B., M. G. Schlax, M. H. Freilich, and R. F. Milliff, 2004: Satellite measurements reveal persistent small-scale features in ocean winds. *Science*, **303**, 978–983, doi:10.1126/science.1091901.

——, ——, and R. M. Samelson, 2007: Summertime coupling between sea surface temperature and wind stress in the California Current System. *J. Phys. Oceanogr.*, **37**, 495–517, doi:10.1175/JPO3025.1.

——, ——, and ——, 2011: Global observations of nonlinear mesoscale eddies. *Prog. Oceanogr.*, **91**, 167–216, doi:10.1016/j.pocean.2011.01.002.

Chou, M.-D., and M. J. Suarez, 1999: A solar radiation parameterization for atmospheric studies. NASA Tech. Rep. 104606, 51 pp. [Available online at http://ntrs.nasa.gov/search.jsp?R=19990060930.]

Colas, F., X. Capet, J. C. McWilliams, and Z. Li, 2013: Mesoscale eddy buoyancy flux and eddy-induced circulation in Eastern Boundary Currents. *J. Phys. Oceanogr.*, **43**, 1073–1095, doi:10.1175/JPO-D-11-0241.1.

Cornillon, P., and K. Park, 2001: Warm core ring velocities inferred from NSCAT. *Geophys. Res. Lett.*, **28**, 575–578, doi:10.1029/2000GL011487.

Dawe, J. T., and L. Thompson, 2006: Effect of ocean surface currents on wind stress, heat flux, and wind power input to the ocean. *Geophys. Res. Lett.*, **33**, L09604, doi:10.1029/2006GL025784.

Debreu, L., P. Marchesiello, P. Penven, and G. Cambon, 2012: Two-way nesting in split–explicit ocean models: Algorithms, implementation and validation. *Ocean Model.*, **49–50**, 1–21, doi:10.1016/j.ocemod.2012.03.003.

Desbiolles, F., B. Blanke, A. Bentamy, and C. Roy, 2016: Response of the Southern Benguela upwelling system to fine-scale modifications of the coastal wind. *J. Mar. Syst.*, **156**, 46–55, doi:10.1016/j.jmarsys.2015.12.002.

Dewar, W. K., and G. R. Flierl, 1987: Some effects of the wind on rings. *J. Phys. Oceanogr.*, **17**, 1653–1667, doi:10.1175/1520-0485(1987)017<1653:SEOTWO>2.0.CO;2.

Ducet, N., P.-Y. Le Traon, and G. Reverdin, 2000: Global high-resolution mapping of ocean circulation from TOPEX/Poseidon and ERS-1 and-2. *J. Geophys. Res.*, **105**, 19 477–19 498, doi:10.1029/2000JC900063.

Duhaut, T. H., and D. N. Straub, 2006: Wind stress dependence on ocean surface velocity: Implications for mechanical energy input to ocean circulation. *J. Phys. Oceanogr.*, **36**, 202–211, doi:10.1175/JPO2842.1.

Eden, C., and H. Dietze, 2009: Effects of mesoscale eddy/wind interactions on biological new production and eddy kinetic energy. *J. Geophys. Res.*, **114**, C05023, doi:10.1029/2008JC005129.

Edwards, K. A., A. M. Rogerson, C. D. Winant, and D. P. Rogers, 2001: Adjustment of the marine atmospheric boundary layer to a coastal cape. *J. Atmos. Sci.*, **58**, 1511–1528, doi:10.1175/1520-0469(2001)058<1511:AOTMAB>2.0.CO;2.

FAO, 2009: The state of world fisheries and aquaculture 2008. FAO Rep., 196 pp. [Available online at ftp://ftp.fao.org/docrep/fao/011/i0250e/i0250e.pdf.]

Gaube, P., D. B. Chelton, P. G. Strutton, and M. J. Behrenfeld, 2013: Satellite observations of chlorophyll, phytoplankton biomass, and Ekman pumping in nonlinear mesoscale eddies. *J. Geophys. Res. Oceans*, **118**, 6349–6370, doi:10.1002/2013JC009027.

——, ——, R. M. Samelson, M. G. Schlax, and L. W. O'Neill, 2015: Satellite observations of mesoscale eddy-induced Ekman pumping. *J. Phys. Oceanogr.*, **45**, 104–132, doi:10.1175/JPO-D-14-0032.1.

Gruber, N., Z. Lachkar, H. Frenzel, P. Marchesiello, M. Münnich, J. C. McWilliams, T. Nagai, and G.-K. Plattner, 2011: Eddy-induced reduction of biological production in eastern

boundary upwelling systems. *Nat. Geosci.*, **4**, 787–792, doi:10.1038/ngeo1273.

Hong, S.-Y., and J.-O. J. Lim, 2006: The WRF Single-Moment 6-class Microphysics scheme (WSM6). *J. Korean Meteor. Soc.*, **42**, 129–151.

——, Y. Noh, and J. Dudhia, 2006: A new vertical diffusion package with an explicit treatment of entrainment processes. *Mon. Wea. Rev.*, **134**, 2318–2341, doi:10.1175/MWR3199.1.

Hughes, C. W., and C. Wilson, 2008: Wind work on the geostrophic ocean circulation: An observational study of the effect of small scales in the wind stress. *J. Geophys. Res.*, **113**, C02016, doi:10.1029/2007JC004371.

Jin, X., C. Dong, J. Kurian, J. C. McWilliams, D. B. Chelton, and Z. Li, 2009: SST–wind interaction in coastal upwelling: Oceanic simulation with empirical coupling. *J. Phys. Oceanogr.*, **39**, 2957–2970, doi:10.1175/2009JPO4205.1.

Jousse, A., A. Hall, F. Sun, and J. Teixeira, 2016: Causes of WRF surface energy fluxes biases in a stratocumulus region. *Climate Dyn.*, **46**, 571–584, doi:10.1007/s00382-015-2599-9.

Kurian, J., F. Colas, X. Capet, J. C. McWilliams, and D. B. Chelton, 2011: Eddy properties in the California Current System. *J. Geophys. Res.*, **116**, C08027, doi:10.1029/2010JC006895.

Large, W. B., 2006: Surface fluxes for practitioners of global ocean data assimilation. *Ocean Weather Forecasting*. E. P. Chassignet and J. Verron, Eds., Springer, 229–270, doi:10.1007/1-4020-4028-8_9.

Large, W. G., and S. Pond, 1981: Open ocean momentum flux measurements in moderate to strong winds. *J. Phys. Oceanogr.*, **11**, 324–336, doi:10.1175/1520-0485(1981)011<0324:OOMFMI>2.0.CO;2.

——, J. C. McWilliams, and S. C. Doney, 1994: Oceanic vertical mixing: A review and a model with a nonlocal boundary layer parameterization. *Rev. Geophys.*, **32**, 363–404, doi:10.1029/94RG01872.

Lathuilière, C., V. Echevin, M. Lévy, and G. Madec, 2010: On the role of the mesoscale circulation on an idealized coastal upwelling ecosystem. *J. Geophys. Res.*, **115**, C09018, doi:10.1029/2009JC005827.

Lemarié, F., 2015: Numerical modification of atmospheric models to include the feedback of oceanic currents on air–sea fluxes in ocean–atmosphere coupled models. INRIA Grenoble - Rhône-Alpes Tech. Rep. RT-464, 10 pp. [Available online at https://hal.inria.fr/hal-01184711/document.]

Lorenz, E. N., 1955: Available potential energy and the maintenance of the general circulation. *Tellus*, **7A**, 157–167, doi:10.1111/j.2153-3490.1955.tb01148.x.

Marchesiello, P., J. C. McWilliams, and A. Shchepetkin, 2001: Open boundary conditions for long-term integration of regional oceanic models. *Ocean Modell.*, **3**, 1–20, doi:10.1016/S1463-5003(00)00013-5.

——, ——, and ——, 2003: Equilibrium structure and dynamics of the California Current System. *J. Phys. Oceanogr.*, **33**, 753–783, doi:10.1175/1520-0485(2003)33<753:ESADOT>2.0.CO;2.

Martin, A. P., and K. J. Richards, 2001: Mechanisms for vertical nutrient transport within a North Atlantic mesoscale eddy. *Deep-Sea Res. II*, **48**, 757–773, doi:10.1016/S0967-0645(00)00096-5.

Mason, E., J. Molemaker, A. F. Shchepetkin, F. Colas, J. C. McWilliams, and P. Sangrà, 2010: Procedures for offline grid nesting in regional ocean models. *Ocean Modell.*, **35**, 1–15, doi:10.1016/j.ocemod.2010.05.007.

McGillicuddy, D. J., 2015: Formation of intrathermocline lenses by eddy–wind interaction. *J. Phys. Oceanogr.*, **45**, 606–612, doi:10.1175/JPO-D-14-0221.1.

——, and Coauthors, 2007: Eddy/wind interactions stimulate extraordinary mid-ocean plankton blooms. *Science*, **316**, 1021–1026, doi:10.1126/science.1136256.

Minobe, S., A. Kuwano-Yoshida, N. Komori, S.-P. Xie, and R. J. Small, 2008: Influence of the Gulf Stream on the troposphere. *Nature*, **452**, 206–209, doi:10.1038/nature06690.

Nagai, T., N. Gruber, H. Frenzel, Z. Lachkar, J. C. McWilliams, and G.-K. Plattner, 2015: Dominant role of eddies and filaments in the offshore transport of carbon and nutrients in the California Current System. *J. Geophys. Res. Oceans*, **120**, 5318–5341, doi:10.1002/2015JC010889.

Nakanishi, M., and H. Niino, 2006: An improved Mellor–Yamada Level-3 model: Its numerical stability and application to a regional prediction of advection fog. *Bound.-Layer Meteor.*, **119**, 397–407, doi:10.1007/s10546-005-9030-8.

Oerder, V., F. Colas, V. Echevin, S. Masson, C. Hourdin, S. Jullien, G. Madec, and F. Lemarié, 2016: Mesoscale SST–wind stress coupling in the Peru–Chile current system: Which mechanisms drive its seasonal variability? *Climate Dyn.*, doi:10.1007/s00382-015-2965-7, in press.

Park, H., D. Lee, W.-P. Jeon, S. Hahn, J. Kim, J. Kim, J. Choi, and H. Choi, 2006: Drag reduction in flow over a two-dimensional bluff body with a blunt trailing edge using a new passive device. *J. Fluid Mech.*, **563**, 389–414, doi:10.1017/S0022112006001364.

Park, S., and C. S. Bretherton, 2009: The University of Washington shallow convection and moist turbulence schemes and their impact on climate simulations with the Community Atmosphere Model. *J. Climate*, **22**, 3449–3469, doi:10.1175/2008JCLI2557.1.

Perlin, N., E. D. Skyllingstad, R. M. Samelson, and P. L. Barbour, 2007: Numerical simulation of air–sea coupling during coastal upwelling. *J. Phys. Oceanogr.*, **37**, 2081–2093, doi:10.1175/JPO3104.1.

——, ——, and ——, 2011: Coastal atmospheric circulation around an idealized cape during wind-driven upwelling studied from a coupled ocean–atmosphere model. *Mon. Wea. Rev.*, **139**, 809–829, doi:10.1175/2010MWR3372.1.

Renault, L., B. Dewitte, M. Falvey, R. Garreaud, V. Echevin, and F. Bonjean, 2009: Impact of atmospheric coastal jet off central Chile on sea surface temperature from satellite observations (2000–2007). *J. Geophys. Res.*, **114**, C08006, doi:10.1029/2008JC005083.

——, and Coauthors, 2012: Upwelling response to atmospheric coastal jets off central Chile: A modeling study of the October 2000 event. *J. Geophys. Res.*, **117**, C02030, doi:10.1029/2011JC007446.

——, A. Hall, and J. C. McWilliams, 2015: Orographic shaping of U.S. West Coast wind profiles during the upwelling season. *Climate Dyn.*, **46**, 273–289, doi:10.1007/s00382-015-2583-4.

——, C. Deutsch, J. C. McWilliams, H. Frenzel, J. H. Liang, and F. Colas, 2016: Partial decoupling of primary productivity from upwelling in the California Current System. *Nat. Geosci.*, in press.

Saha, S., and Coauthors, 2010: The NCEP Climate Forecast System Reanalysis. *Bull. Amer. Meteor. Soc.*, **91**, 1015–1057, doi:10.1175/2010BAMS3001.1.

Samelson, R., M. Schlax, and D. Chelton, 2014: Randomness, symmetry, and scaling of mesoscale eddy life cycles. *J. Phys. Oceanogr.*, **44**, 1012–1029, doi:10.1175/JPO-D-13-0161.1.

Sandwell, D. T., and W. H. Smith, 1997: Marine gravity anomaly from Geosat and ERS 1 satellite altimetry. *J. Geophys. Res.*, **102**, 10 039–10 054, doi:10.1029/96JB03223.

Scott, R. B., and Y. Xu, 2009: An update on the wind power input to the surface geostrophic flow of the World Ocean. *Deep-Sea Res. I*, **56**, 295–304, doi:10.1016/j.dsr.2008.09.010.

Seo, H., A. J. Miller, and J. R. Norris, 2016: Eddy–wind interaction in the California Current System: Dynamics and impacts. *J. Phys. Oceanogr.*, **46**, 439–459, doi:10.1175/JPO-D-15-0086.1.

Shchepetkin, A. F., and J. C. McWilliams, 2005: The regional oceanic modeling system (ROMS): A split-explicit, free-surface, topography-following-coordinate oceanic model. *Ocean Modell.*, **9**, 347–404, doi:10.1016/j.ocemod.2004.08.002.

——, and ——, 2009: Correction and commentary for "Ocean forecasting in terrain-following coordinates: Formulation and skill assessment of the regional ocean modeling system" by Haidvogel et al., J. Comp. Phys. 227, pp. 3595–3624. *J. Comput. Phys.*, **228**, 8985–9000, doi:10.1016/j.jcp.2009.09.002.

Skamarock, W., J. Klemp, J. Dudhia, D. Gill, and D. Barker, 2008: A description of the Advanced Research WRF version 3. NCAR. Tech. Note NCAR/TN-475+STR, doi:10.5065/D68S4MVH.

Spall, M. A., 2007: Midlatitude wind stress–sea surface temperature coupling in the vicinity of oceanic fronts. *J. Climate*, **20**, 3785–3801, doi:10.1175/JCLI4234.1.

Wang, W., and R. X. Huang, 2004: Wind energy input to the Ekman layer. *J. Phys. Oceanogr.*, **34**, 1267–1275, doi:10.1175/1520-0485(2004)034<1267:WEITTE>2.0.CO;2.

Watanabe, M., and T. Hibiya, 2002: Global estimates of the wind-induced energy flux to inertial motions in the surface mixed layer. *Geophys. Res. Lett.*, **29**, 64-1–64-3, doi:10.1029/2001GL014422.

Zhang, C., Y. Wang, and K. Hamilton, 2011: Improved representation of boundary layer clouds over the Southeast Pacific in ARW-WRF using a modified Tiedtke cumulus parameterization scheme. *Mon. Wea. Rev.*, **139**, 3489–3513, doi:10.1175/MWR-D-10-05091.1.